



## Circadian rhythm orthologs drive pulses of heterochronic miRNA transcription in *C. elegans*

Brian Kinney, Shubham Sahu, Natalia Stec, Kelly Hills-Muckey, Dexter W Adams, Jing Wang, Matt Jaremako, Leemor Joshua-Tor, Wolfgang Keil, Christopher M Hammell

### ► To cite this version:

Brian Kinney, Shubham Sahu, Natalia Stec, Kelly Hills-Muckey, Dexter W Adams, et al.. Circadian rhythm orthologs drive pulses of heterochronic miRNA transcription in *C. elegans*. 2022. hal-03878871

**HAL Id: hal-03878871**

**<https://hal.science/hal-03878871>**

Preprint submitted on 30 Nov 2022

**HAL** is a multi-disciplinary open access archive for the deposit and dissemination of scientific research documents, whether they are published or not. The documents may come from teaching and research institutions in France or abroad, or from public or private research centers.

L'archive ouverte pluridisciplinaire **HAL**, est destinée au dépôt et à la diffusion de documents scientifiques de niveau recherche, publiés ou non, émanant des établissements d'enseignement et de recherche français ou étrangers, des laboratoires publics ou privés.

# **Circadian rhythm orthologs drive pulses of heterochronic miRNA transcription in *C. elegans***

Brian Kinney<sup>1\*</sup>, Shubham Sahu<sup>2\*</sup>, Natalia Stec<sup>1</sup>, Kelly Hills-Muckey<sup>1</sup>, Dexter W. Adams<sup>3,4</sup>, Jing Wang<sup>1</sup>, Matt Jaremako<sup>3</sup>, Leemor Joshua-Tor<sup>3</sup>, Wolfgang Keil<sup>2,†</sup>, Christopher M. Hammell<sup>1,†</sup>

<sup>1</sup>Cold Spring Harbor Laboratory, Cold Spring Harbor, NY 11724, USA.

<sup>2</sup>Institut Curie, Université PSL, Sorbonne Université, CNRS UMR168 Laboratoire Physico Chimie Curie, 75005 Paris, France.

<sup>3</sup>Howard Hughes Medical Institute, W. M. Keck Structural Biology Laboratory, Cold Spring Harbor Laboratory, Cold Spring Harbor, NY, 11724, USA

<sup>4</sup>Graduate Program in Genetics, Stony Brook University; Stony Brook, NY 11794, USA

\*These authors contributed equally

<sup>†</sup>Correspondence: wolfgang.keil@curie.fr (W.K.); chammell@cshl.edu (C.M.H.) (lead contact)

**Abstract:** The *C. elegans* transcriptome exhibits reproducible, periodic patterns that are phase-locked with features of the larval molting cycle, but the gene regulatory networks underlying this interdependency are unknown. We show here that repeated transcriptional pulses of the *lin-4* temporal patterning miRNA are generated by cooperative binding between the *C. elegans* orthologs of master circadian regulators Rev-Erb and ROR to elements upstream of the *lin-4* gene. Remarkably, the precise timing and length of *lin-4* transcriptional pulses are dictated by the phased overlap of NHR-85<sup>Rev-Erb</sup> and NHR-23<sup>ROR</sup> temporal expression patterns. We also demonstrate that LIN-42<sup>Period</sup> functions in a similar capacity to its circadian orthologs to negatively regulate periodic transcription but does so by limiting the duration of NHR-85<sup>Rev-Erb</sup>/NHR-23<sup>ROR</sup> cooperative activity at the *lin-4* gene.

**Summary:** Orthologs of circadian clock genes generate repeated transcriptional pulses of developmental timing genes in *C. elegans*

Ontogenesis is an inherently dynamic process during which the timing and sequence of developmental events must be organized through coordinated patterns of gene expression. The four larval stages of *C. elegans* are characterized by stage-specific patterns of cell division, cell differentiation, and cuticle formation that occur during intermolt periods (1). Classical forward genetic approaches have identified several highly conserved temporal selector genes that combinatorially program stage-specific patterns of cell fate specification during post-embryonic development (2). Transitions through successive stage-specific developmental cell fate programs are mediated by the accumulation of several microRNAs (miRNAs) that post-transcriptionally regulate the expression of their temporal selector gene targets (3). Importantly, the activity of these regulatory RNAs within this so-called heterochronic gene regulatory network (GRN) is dosage sensitive, meaning that abnormally lower or higher dosages of heterochronic miRNAs result in wholesale skipping or reiteration of discrete stage-specific developmental programs (3-7). The sequential expression of heterochronic miRNAs therefore couple temporal cell-fate progression to the repetitive larval molting cycles.

Approximately 20% of the *C. elegans* transcriptome exhibits reproducible, periodic expression patterns that are phase-locked with features of the molting cycle (8-11). These patterns and their coordination are genetically controlled, occur with exquisite robustness regardless of environmental and physiological stresses, and are independent of life-history (8-11) suggesting that a system patterns gene expression to orchestrate the temporal coordination of developmental processes. Remarkably, the transcription of heterochronic miRNAs is also coupled to the larval molting cycles (6, 7, 10, 12). While several transcription factors (TFs) have been implicated in controlling heterochronic miRNA transcription (13-18), we lack mechanistic understanding of how miRNA gene expression is coupled to the molting clock, and how the precise transcriptional dynamics of microRNA loci - including pulse amplitude, duration, and phase of expression within each cycle - is controlled to tightly govern the critical dynamics of miRNA dosage as development progresses.

## **Pulsatile transcription of *lin-4* is coordinated with larval stage progression**

Within the heterochronic GRN, the *lin-4* gene encodes a miRNA that controls the transition from L1- to L2-stage patterns of gene expression (19) and is expressed periodically throughout all larval stages (11). To directly measure *lin-4* transcriptional kinetics, we implemented the MS2/MCP-GFP tethering system, which exploits the natural affinity between RNA loops derived from MS2 bacteriophage and a co-expressed MS2 coat protein fused to green fluorescent protein (MCP-GFP)(20). By genetically encoding the MS2 hairpins within a gene of interest, nascent RNAs can be directly imaged in living cells through their ability concentrate MCP-GFP at the sites of RNA synthesis



(Fig. 1A). To visualize *lin-4* transcription, we generated a ~4kb transgene harboring the *lin-4* precursor RNA followed by 24 copies of a synthetic MS2 hairpin upstream of the polyadenylation sequences and the upstream regulatory information required to drive normal *lin-4* transcription (11) (fig. S1A)(21). This transgene fully rescues the developmental phenotypes associated with the *lin-4* null allele (*lin-4(e912)*) (fig. S1). We also drove ubiquitous expression of MCP fused to GFP (MCP-GFP) to detect MS2-tagged RNAs, and a histone H2B subunit (HIS-58) fused to mCherry to locate nuclei (fig. S1A). Examination of L3-staged transgenic animals revealed that dynamic *lin-4* expression (MCP-GFP foci) occurred from each *lin-4::MS2* locus in somatic tissue types known to transcribe *lin-4* (Fig. 1B). MCP-GFP foci were never observed in developing embryos (n > 50) or in starvation arrested L1 larva (n = 23); consistent with the activation of *lin-4* transcription after the initiation of larval development (4).

Next, we used our microfluidics platform to perform live spinning-disk confocal microscopy of developing *C. elegans* larvae harboring *lin-4::24xMS2/MCP-GFP* system (11, 22). We focused on quantifying expression dynamics in hypodermal cells (seam, hyp7 and vulval precursor cells (VPCs)) where the timing of transcriptional activity within a given larval stage can be accurately assessed in relation to the occurrence of precisely timed stage-specific cell division patterns (1). We first screened for periods of *lin-4* transcriptional activity by imaging at 15min time intervals from early first larval stage (L1) to mid L4 stages (~60h) (n>10). This revealed that *lin-4::24xMS2* transcription was highly pulsatile, with a single transcriptional episode of ~45-90min in each cell during each larval stage, followed by extremely long periods of inactivity (>8hrs at 20°C) (Fig. 1C). Transcriptional activation across cells within the entire hypodermis was highly concordant, exhibiting similar transcriptional on and off times for all *lin-4::24xMS2* loci (Fig. 1E). For instance, during the mid-L3 stage, the appearance of *lin-4::24xMS2* expression throughout the hypodermis generally occurred within minutes of the first VPC divisions (P3.p or P4.p) and were completed by the divisions of P5.p-P7.p (n = 15) (Fig. 1C).

Based on these observations, we performed short-term imaging time courses (<6h) at 4min intervals in staged larvae to capture transcriptional epochs at high temporal resolution. During transcriptional episodes, we detected near synchronous accumulation of MCP-GFP foci at each hypodermal *lin-4::24xMS2* locus for 60-90 minutes (Fig. 1D-E, Suppl. Movie 1,2) (>15 animals). We found no signs of “bursty” transcription (23) as loci generally stayed on for the entire transcriptional episode (Suppl. Movie 1,2). These features were independent of the number of *lin-4::24xMS2* loci per nucleus as cell types that undergo endoreduplication (i.e., hyp7 cells) exhibited MCP-GFP foci dynamics indistinguishable from diploid cells (Fig. 1D). The dynamic features of *lin-4::24xMS2* expression in hypodermal cells were similar across different developmental stages (Fig. 1E)

suggesting that the same regulatory programs controlling *lin-4* transcription were repeated at each larval stage. Finally, the pulsatile nature of transcriptional activation occurred in a broad array of additional cell types that normally express *lin-4*. These include pharyngeal muscles and intestinal cells in which the phase of transcriptional induction is shifted later compared to patterns observed in hypodermal cells and the duration of pulses are extended (fig. S2).

## **NHR-85<sup>Rev-Erb</sup> and NHR-23<sup>ROR</sup> interact with the regulatory regions that control repetitive *lin-4* transcription**

We previously demonstrated that highly pulsatile transcription from the *lin-4* locus is dependent on the upstream *lin-4* PCE (pulse control element) (11). To identify candidate TFs that bind this conserved regulatory sequence, we performed a yeast-one-hybrid screen using the entire 514bp *lin-4* PCE as bait and identified three TFs (BLMP-1, NHR-23 and NHR-85) (Fig. 2A). BLMP-1 controls the amplitude of *lin-4* expression and functions as a pioneer factor to decompact the *lin-4* locus throughout development (11). *nhr-85* and *nhr-23* encode two nuclear hormone receptors (NHRs) that are the closest nematode orthologs of human circadian TFs Rev-Erb and ROR, respectively (Fig. 2B). Analysis of publicly available ChIP-seq data indicated that all three proteins interact *in vivo* with *lin-4* regulatory sequences, which contain putative consensus binding sites for each TF (Fig. 2A). Furthermore, NHR-85<sup>Rev-Erb</sup>, NHR-23<sup>ROR</sup> and BLMP-1 binding sites are highly overlapping and enriched in the promoters of numerous cyclically expressed protein coding genes and heterochronic miRNAs (fig. S3) (table S1 and S2).

## **NHR-85<sup>Rev-Erb</sup> and NHR-23<sup>ROR</sup> heterodimerize and bind cooperatively *lin-4* regulatory elements**

Nuclear hormone receptors often bind cooperatively as homo- or hetero-dimeric complexes at closely spaced cis-regulatory DNA elements (24-26). Several features of NHR-85<sup>Rev-Erb</sup>, NHR-23<sup>ROR</sup> and the *lin-4* PCE suggest that this may also be the case for *lin-4* transcription. First, NHR-85<sup>Rev-Erb</sup> and NHR-23<sup>ROR</sup> share significant sequence homology within their ZnF C4-type DNA-binding domains implicated in DNA interactions and dimerization, suggesting they may function at similar binding sites (Fig. 2C)(27). Second, we found that NHR-85<sup>Rev-Erb</sup> and NHR-23<sup>ROR</sup> could bind to form heterodimers in yeast two-hybrid assays, which could be reconstituted *in vitro* with a binding affinity of 5.8 +/- 2.2 nM K<sub>D</sub> (Fig. 2D,E). Third, sequences within the PCE element contain direct repeats of a GGTC A that are contained in predicted binding sites of NHR-85<sup>Rev-Erb</sup> and NHR-23<sup>ROR</sup> (Fig. 2F and G). Fourth, while NHR-23<sup>ROR</sup> alone could bind a DNA fragment at high TF/DNA molar ratios (fig. S4A,B), we found that

DNA binding assays containing concentrations of NHR-23<sup>ROR</sup> that are insufficient to bind the PCE alone are dramatically stimulated by the addition of NHR-85<sup>Rev-Erb</sup> (Fig. 2H,I). NHR-85<sup>Rev-Erb</sup> alone was unable to reproducibly bind any *lin-4* PCE DNA fragments (fig. S4C). Finally, the cooperative binding of NHR-85<sup>Rev-Erb</sup> and NHR-23<sup>ROR</sup> to *lin-4* enhancer fragments requires the presence of both conserved GGTCA direct repeats, suggesting these NHRs bind closely spaced regulatory elements as a heterodimer (Fig. 2H).

### **NHR-85<sup>Rev-Erb</sup>, NHR-23<sup>ROR</sup>, and LIN-42<sup>Period</sup> expression is phased during each larval stage**

Previous studies indicate that LIN-42<sup>Period</sup>, the *C. elegans* ortholog of the circadian Period protein, negatively regulates the expression of *lin-4* throughout post-embryonic development (7, 12, 28). Given the roles of mammalian Period, ROR, Rev-Erb in controlling circadian gene regulation in mouse and human, we examined potential regulatory relationships between the *C. elegans* orthologs of these genes in the context of *lin-4* transcription. Single-cell expression analysis indicates that *nhr-85* and *nhr-23* mRNAs are enriched in hypodermal and glial cells while *lin-42* is broadly expressed (Fig. 3A)(29). *nhr-85* transcription initiates from an L1-stage arrest with a pulse of transcription that is followed by a monotonic expression pattern at subsequent larval stages (Fig. 3B). In contrast, *nhr-23* and *lin-42* mRNAs exhibit phased, high-amplitude oscillatory patterns of expression (Fig. 3B).

We next explored the temporal dynamics of NHR-85<sup>Rev-Erb</sup>, NHR-23<sup>ROR</sup> and LIN-42<sup>Period</sup> protein by quantifying the expression of endogenously-tagged alleles of each gene during the L4 stage, in which the evenly-spaced, stereotyped morphological changes in vulval morphogenesis can be directly correlated with developmental age (30). Consistent with previous characterization of NHR-23<sup>ROR</sup> and LIN-42<sup>Period</sup> expression patterns determined using reporter transgenes (31, 32), each of our endogenous reporters was expressed dynamically in hypodermal cells with a single peak of expression that roughly matches the phased expression of their mRNAs (Fig. 3C). In contrast to the flat expression of *nhr-85* transcripts in L2-L4 stages of development, we found that NHR-85<sup>Rev-Erb::GFP</sup> expression was highly dynamic, indicating substantial post-transcriptional regulation of NHR-85<sup>Rev-Erb</sup> expression. Specifically, peak expression of NHR-85<sup>Rev-Erb::GFP</sup> occurs at ecdysis (shortly before NHR-23<sup>ROR::mScarlet</sup> onset), becomes undetectable by the L4.3 stage of development, and resumes at the L4.6 stage in an antiphasic manner to the expression pattern of LIN-42<sup>Period::YFP</sup> (Fig. 3C). Highly similar phased expression patterns of these proteins are also maintained in L4-staged vulval tissues (Fig. 3D) as well as in L3-staged hypodermal cells and VPCs (Fig. 4).

## **The temporal overlap in NHR-85<sup>Rev-Erb</sup> and NHR-23<sup>ROR</sup> expression correlates with *lin-4* transcriptional pulses**

The overlap in NHR-85<sup>Rev-Erb</sup>::GFP and NHR-23<sup>ROR</sup>::mScarlet expression during the L4 stage lasts 60-90min (L4.2-L4.3) (Fig. 3D), the approximate duration of *lin-4* transcription in hypodermal cells and VPCs at this same stage (Fig. 1D,E)(30). To compare the timing of these events, we examined MCP-GFP localization in vulval cells during the L3 stage, where the rapid, stereotyped vulval cell division patterns (22) enable precise determination of the timing of *lin-4::24xMS2* transcription and TF dynamics. We found a striking correspondence between NHR-85<sup>Rev-Erb</sup> and NHR-23<sup>ROR</sup> co-expression and *lin-4::24xMS2* transcription (Fig. 4). Specifically, while the expression of both nuclear receptors is phased, the transient expression of the *lin-4::24xMS2* transgene only occurs during the brief period when both NHR proteins are expressed in VPCs (Fig. 4A). This almost perfect correspondence is also maintained in hypodermal cells during this transcriptional cycle where both NHR-85<sup>Rev-Erb</sup> expression and MCP-GFP foci are diminished near the completion of the first round of VPC divisions (Fig. 1E and 3D). Importantly, the timing of NHR-85<sup>Rev-Erb</sup> downregulation is also concurrent with onset of LIN-42<sup>Period</sup> expression in VPCs and hypodermal cells (Fig. 3D and 4A). The phased expression patterns of all TFs and the dynamics of MCP-GFP foci accumulation are also conserved in the L4 stage of development (Fig. 4B). This indicates that the timing and duration of *lin-4* transcriptional pulses are likely encoded by the dynamic expression patterns of these TFs (Fig. 4C).

## **LIN-42<sup>Period</sup> regulates NHR-85<sup>Rev-Erb</sup> levels to modulate the amplitude and duration of *lin-4* transcription**

Mutations in *lin-42<sup>Period</sup>* produce late temporal patterning defects including precocious expression of adult-specific genes in the L4 stage (Fig. 5A) (6, 7, 33). Mammalian Period orthologs have been shown to interact with multiple NHRs and modulate their transcriptional activity (34). To determine if LIN-42<sup>Period</sup> could physically interact with other *C. elegans* NHRs, we systematically probed LIN-42<sup>Period</sup> interactions with a majority of the of *C. elegans* NHRs (243 of 284) using two-hybrid assays. We identified 66 *C. elegans* NHRs that could interact with LIN-42<sup>Period</sup> in yeast (fig. S5A,B), including orthologs of Rev-Erb(NHR-85)(Fig. 5B), HNF4a(NHR-14, NHR-69) and PPAR $\alpha$ (NHR-119), indicating evolutionary conservation of physical interactions between *Period* orthologs and related NHRs (Fig. S5A-B)(34). We mapped the domains of LIN-42<sup>Period</sup> that are required for NHR-85<sup>Rev-Erb</sup> binding and found that a minimal 51aa fragment present in both major LIN-42<sup>Period</sup> isoforms is sufficient to mediate interactions (Fig. 5A). This domain is distinct from the

interaction motifs implicated in mammalian Per2 and Rev-Erb (34). Neither LIN-42<sup>Period</sup> isoform interacts with NHR-23<sup>ROR</sup> in two-hybrid assays (Fig. 5A).

Given the physical interaction between NHR-85<sup>Rev-Erb</sup> and LIN-42<sup>Period</sup>, we asked whether NHR-85<sup>Rev-Erb</sup> expression was required for the precocious phenotypes seen in *lin-42(lf)* mutants (*lin-42(n1089)*). We found that *lin-42(lf)* heterochronic phenotypes are partially ameliorated by removing *nhr-85* function. Specifically, precocious expression of *col-19::GFP* in both seam and hyp7 cells observed in *lin-42(lf)* mutants is suppressed by *nhr-85* deletion; leaving weak expression in seam cells in double mutants, while precocious deposition of adult alae was not suppressed (Fig. 5A). To examine whether LIN-42<sup>Period</sup> regulates NHR-85<sup>Rev-Erb</sup> temporal dynamics, we compared the dynamics of NHR-85<sup>Rev-Erb</sup>::GFP (and NHR-23<sup>ROR</sup>::mScarlet) expression in wild-type and *lin-42(lf)* mutants. We found that the expression of NHR-85<sup>Rev-Erb</sup> is altered in two ways by a *lin-42(lf)* mutation: First, expression of NHR-85<sup>Rev-Erb</sup>::GFP is ~2.3x more abundant at the beginning of the L4 stage in *lin-42* mutants when compared to wild-type animals (Fig. 5C and D). Importantly, the periodic dampening of NHR-85<sup>Rev-Erb</sup> expression at the L4.2 stage observed in wild-type animals (Fig. 3C,D) is altered in *lin-42(lf)* mutants and NHR-85<sup>Rev-Erb</sup>::GFP expression perdures into the L4.4 stage (Fig. 5C,D). Mutations in *lin-42* do not alter the onset or duration of NHR-23<sup>ROR</sup>::mScarlet accumulation in hypodermal or vulval cells.

Our results suggest that timing of *lin-4* transcriptional pulses is defined by the brief co-expression of NHR-85<sup>Rev-Erb</sup> and NHR-23<sup>ROR</sup> (Fig. 4C). We hypothesized that the corresponding increase in *lin-4* expression levels previously observed in *lin-42(lf)* mutants (6, 7) likely result from alterations in *lin-4* transcription associated with mis-regulation of NHR-85<sup>Rev-Erb</sup> expression. To test this, we examined expression of MCP-GFP foci throughout the L3 stage and found that, while a majority of wild-type seam cells fire a single time (76%; 66 foci), the percentage of seam cells that exhibit detectable *lin-4* transcription is dramatically increased in *lin-42* mutants (100%; 58 foci). This indicates that *lin-42* normally dampens *lin-4* transcriptional pulses in wild-type animals. In addition to elevating the likelihood *lin-4::24xMS2* transcription is above a threshold sufficient to generate measurable MCP-GFP foci, *lin-42(lf)* mutations lead to an increase in the intensity of MCP-GFP foci indicating that LIN-42<sup>Period</sup> normally also limits Pol II loading at the *lin-4* locus (Fig. 5E). Time course experiments revealed that overall duration of detectable transcription in seam cells is ~2.2 times longer in *lin-42* mutants compared to wild-type (Fig. 5E). Consistent with our hypothesis that the duration of *lin-4* transcription is dependent on the duration of NHR-85<sup>Rev-Erb</sup> expression, transcriptional onset of *lin-4* occurs earlier in *lin-42* mutants and inappropriately extends through both the first and second Pn.p divisions (Fig. 5F).



While *nhr-85(0)* mutants do not miss-express *col-19::GFP* (Fig. 5A), high-resolution imaging experiments monitoring VPC divisions and *lin-4::24xMS2* expression indicate that two features of developmental timing are altered in *nhr-85(0)* mutants. Transcriptional pulses of *lin-4::24xMS2* are both robust and concordant in adjacent wild-type VPCs (Fig. 5G). In contrast, MCP-GFP foci in *nhr-85(0)* mutants begin to accumulate at the same relative phase of L3-stage VPC development but are dimmer and only transiently observed (Fig. 5G). Second, under isogenic imaging conditions, the rapid and highly coordinated VPC divisions observed in wild-type animals is altered in *nhr-85(0)* mutants with some P5.p and P7.p dividing hours after the first P6.p division (Fig. 5G). These results indicate that NHR-85 functions to enhance the robustness of temporally regulated processes during development and that some level of *lin-4* transcription occurs without NHR-85<sup>Rev-Erb</sup>, perhaps driven by NHR-23<sup>ROR</sup> alone. Consistent with the hypothesis that NHR-23 and NHR-85 function together to control the normal temporal regulation, RNAi-mediated depletion of *nhr-23* activity in wild-type animals using RNAi conditions that do not induce developmental arrest result in mild heterochronic phenotypes (Fig. S6). The penetrance of these phenotypes is enhanced when *nhr-23* is depleted in *nhr-85(0)* animals, indicating that both NHRs also function cooperatively in temporal patterning (Fig. S7).

## Discussion

Most genetic oscillators are composed of auto-regulatory transcriptional/translational feedback loops where transcription of core clock components are self-regulated (35). A prime example of this type of regulatory circuit is the mammalian circadian clock that coordinates anticipatory patterns of gene expression with the day-night cycle. Circadian transcription factors CLOCK and BMAL1 generate rhythmic expression patterns of thousands of clock control genes (CCGs) (36-39) (Fig. 5H). CCGs include two core transcriptional repressors, Period and CRY, which heterodimerize to negatively regulate CLOCK/BMAL1 activity through direct physical interaction. A second set of CCG repressors is encoded by two NHR genes, Rev-Erb and ROR, which dynamically modulate core clock expression through opposing transcriptional activities (Fig. 5H)(40-42). The delays in expression and translation of these sets of negative clock regulators enable this GRN architecture to generate periodic transcriptional patterns of ~24hrs that are entrainable by new light/dark cycles and maintain consistent periodicity in divergent environmental conditions/temperatures (43).

Here, we show that *C. elegans* larvae employ a GRN involving multiple circadian-related genes to couple *lin-4* transcriptional pulses to the larval molting cycle (Fig. 5H). The complement of

shared components between the human and *C. elegans* GRNs combined with major differences in their regulatory architecture is remarkable. Primary among these differences is the absence of genes encoding Clock and Bmal1 orthologs in the *C. elegans* genome. We propose here that the worm orthologs of Rev-Erb and ROR, which function in humans in a purely auxiliary capacity to stabilize the expression of core circadian clock components, compose the central transcription factors of the hypodermal developmental clock (Fig. 5H). In contrast to their antagonistic roles in the circadian clock, *C. elegans* NHR-85<sup>Rev-Erb</sup> and NHR-23<sup>ROR</sup> heterodimerize and work cooperatively to promote transcriptional pulses (Fig. 5H). Importantly, we demonstrate that cooperativity between NHR-85<sup>Rev-Erb</sup> and NHR-23<sup>ROR</sup> for binding *lin-4* regulatory elements dictates the timing and duration of *lin-4* transcription and that the duration of these interactions is negatively regulated by LIN-42<sup>Period</sup>. Specifically, LIN-42<sup>Period</sup> binds to NHR-85<sup>Rev-Erb</sup> and controls dynamic nature of its expression. Defects in *lin-42* function result in an increase in Pol II density at the *lin-4* locus and a dramatic increase in the duration of *lin-4* transcriptional pulses by expanding the duration NHR-85<sup>Rev-Erb</sup> and NHR-23<sup>ROR</sup> co-expression. The resulting alterations in *lin-4* dosage (and likely the dosage of additional heterochronic miRNAs) cause precocious heterochronic phenotypes in *lin-42* mutants. This suggests that physical and functional interactions between Period orthologs and conserved NHRs are maintained in both circadian and developmental clock systems and that other *C. elegans* NHRs, in addition to NHR-85<sup>Rev-Erb</sup>, may function in the heterochronic pathway.

While NHR-85<sup>Rev-Erb</sup> and NHR-23<sup>ROR</sup> generate pulses of *lin-4* transcription in the hypodermis, NHR-23<sup>ROR</sup> may coordinate cyclical gene expression patterns with overall animal development (Fig. 2A). *nhr-23* is an essential gene and *nhr-23(0)* animals arrest during late embryogenesis/hatching at a time when oscillatory transcription begins (8, 9, 44). Depletion of NHR-23<sup>ROR</sup> during post-embryonic development results in highly penetrant larval arrest phenotypes (45). These arrests prevent somatic cell proliferation/differentiation, occur at the beginning of each larval stage and correlate with the developmental period where NHR-23<sup>ROR</sup> expression begins (45). While the general suspension of developmental processes in NHR-23<sup>ROR</sup>-depleted animals make it unfeasible to measure direct changes in transcription for individual genes, these arrests resemble post-embryonic developmental checkpoints where somatic cell proliferation and cyclical gene expression patterns (including *lin-4*) are halted during acute food removal/starvation (11, 46). Starvation-induced checkpoints are mediated through regulation of the conserved insulin signaling pathway which generate a variety of sterol-derived hormones (47). These hormones may serve as ligands for individual NHRs and provide a mechanism to organize global patterns of gene expression and regulate the pace of organismal development with the molting cycle.

296

## 297 REFERENCES

- 298 1. J. E. Sulston, H. R. Horvitz, *Developmental biology* **56**, 110-156. (1977).
- 299 2. V. Ambros, H. R. Horvitz, *Science* **226**, 409-416 (1984).
- 300 3. A. E. Rougvie, E. G. Moss, *Curr Top Dev Biol* **105**, 153-180 (2013).
- 301 4. R. Feinbaum, V. Ambros, *Developmental biology* **210**, 87-95. (1999).
- 302 5. M. Li *et al.*, *Developmental cell* **9**, 415-422 (2005).
- 303 6. P. M. Van Wynsberghe, A. E. Pasquinelli, *Worm* **3**, e974453 (2014).
- 304 7. R. Perales *et al.*, *PLoS genetics* **10**, e1004486 (2014).
- 305 8. G.-J. Hendriks *et al.*, *Mol Cell* **53**, 380-392 (2014).
- 306 9. M. W. Meeuse *et al.*, *Mol Syst Biol* **16**, e9498 (2020).
- 307 10. D. h. Kim *et al.*, *Nat Genet* **45**, 1337-1344 (2013).
- 308 11. N. Stec *et al.*, *Curr Biol* **31**, 809-826 e806 (2021).
- 309 12. K. A. McCulloch, A. E. Rougvie, *Proceedings of the National Academy of Sciences of the*  
310 *United States of America* **111**, 15450-15455 (2014).
- 311 13. R. Patel *et al.*, *Elife* **11**, (2022).
- 312 14. C. M. Hammell *et al.*, *PNAS* **106**, 18668-18673 (2009).
- 313 15. A. Bethke *et al.*, *Science* **324**, 95-98 (2009).
- 314 16. M. C. Ow *et al.*, *Genes & development* **22**, 2520-2534 (2008).
- 315 17. S. F. Roush, F. J. Slack, *Developmental biology* **334**, 523-534 (2009).
- 316 18. M. W. M. Meeuse *et al.*, *bioRxiv*, (2022).
- 317 19. R. C. Lee *et al.*, *Cell* **75**, 843-854. (1993).
- 318 20. E. Tutucci *et al.*, *Nat Methods* **15**, 81-89 (2018).
- 319 21. J. R. Bracht *et al.*, *Developmental biology* **348**, 210-221 (2010).
- 320 22. W. Keil *et al.*, *Developmental cell*, (2016).
- 321 23. D. R. Larson *et al.*, *Trends in cell biology* **19**, 630-637 (2009).
- 322 24. B. M. Forman *et al.*, *Cell* **81**, 541-550 (1995).
- 323 25. T. Perlmann *et al.*, *Mol Endocrinol* **10**, 958-966 (1996).
- 324 26. F. Rastinejad *et al.*, *Nature* **375**, 203-211 (1995).
- 325 27. T. P. Burris, *Mol Endocrinol* **22**, 1509-1520 (2008).
- 326 28. P. M. Van Wynsberghe *et al.*, *Developmental biology* **390**, 126-135 (2014).
- 327 29. J. Cao *et al.*, *Science* **357**, 661-667 (2017).
- 328 30. D. Z. L. Mok *et al.*, *BMC developmental biology* **15**, 26 (2015).
- 329 31. M. Jeon *et al.*, *Science* **286**, 1141-1146 (1999).
- 330 32. J. M. Tennessen *et al.*, *Developmental biology* **289**, 30-43 (2006).
- 331 33. J. E. Abrahante *et al.*, *Genetics* **149**, 1335-1351 (1998).
- 332 34. I. Schmutz *et al.*, *Genes Dev* **24**, 345-357 (2010).
- 333 35. B. Novak, J. J. Tyson, *Nat Rev Mol Cell Biol* **9**, 981-991 (2008).
- 334 36. M. K. Bunger *et al.*, *Cell* **103**, 1009-1017 (2000).
- 335 37. J. B. Hogenesch *et al.*, *Proc Natl Acad Sci U S A* **95**, 5474-5479 (1998).
- 336 38. D. P. King *et al.*, *Cell* **89**, 641-653 (1997).
- 337 39. M. Reick *et al.*, *Science* **293**, 506-509 (2001).
- 338 40. N. Preitner *et al.*, *Cell* **110**, 251-260 (2002).
- 339 41. H. R. Ueda *et al.*, *Nature* **418**, 534-539 (2002).
- 340 42. T. K. Sato *et al.*, *Neuron* **43**, 527-537 (2004).
- 341 43. P. Francois *et al.*, *PLoS Comput Biol* **8**, e1002585 (2012).
- 342 44. M. Kostrouchova *et al.*, *PNAS* **98**, 7360-7365 (2001).
- 343 45. L. C. Johnson *et al.*, *bioRxiv*, 2021.2010.2027.465992 (2022).
- 344 46. A. J. Schindler *et al.*, *PLoS genetics* **10**, e1004426 (2014).



345 47. L. R. Baugh, P. J. Hu, *Genetics* **216**, 837-878 (2020).

346

347 **Acknowledgements:**

348 We would like to thank M. Walhout, J. Ward, J. Kimble for strains and reagents and D. Matus and T.  
349 Medwig-Kinney for help with confocal imaging. We would like to also thank G. Sumati for help with  
350 recombinant protein expression. L.J. is an investigator of the Howard Hughes Medical Institute. We  
351 acknowledge T. Medwig-Kinney, C. Vakoc, R. Martienssen, U. Pedmale, and D. Jackson for  
352 suggestions throughout the course of this study.

353 **Funding:**

354 National Institutes of Health R01GM117406 (CMH, NS, KH-M)

355 National Science Foundation 2217560 (CMH, JW)

356 CSHL Cancer Training Grant T32CA148056 (BK)

357 The CNRS ATIP/Avenir program Conseil Regional d'Île de France (DIM ELICIT-AAP-2020 KEIL)  
358 (20002719) (WK)

359 Fondation pour la Recherche Médicale FDT202204015083 (SS)

360 Howard Hughes Medical Institute (LJ, DA, MJ)

361 **Author Contributions:**

362 Conceptualization: CMH, BK, SS, WK

363 Methodology: BK, SS, NS, KH-M, DA, JW, MJ, LJ, WK, CMH

364 Investigation: BK, SS, DA, NS, KH-M, WK, CMH

365 Visualization: CMH, WK, BK, SS

366 Funding acquisition: CMH, WK, JT

367 Project administration: CMH, WK

368 Supervision: CMH, WK, JT

369 Writing – original draft: CMH

370 Writing – review & editing: CMH, WK, BK

371

372 **Competing interests:** All authors declare no competing interests.

373 **Data and materials availability:** Strains and plasmids listed in the Supplementary Materials and  
 374 Methods Section are available through the *Caenorhabditis Genetics* Center or by request to C.M.H..  
 375 The authors affirm that all data necessary for confirming the conclusions of the article are present  
 376 within the article, figures, and tables.

## 377 **Supplementary Materials**

378 Materials and Methods

379 Figs. S1-S6

380 Tables S1-S4

381 References (1-17)

382 Movies S1-S2

383

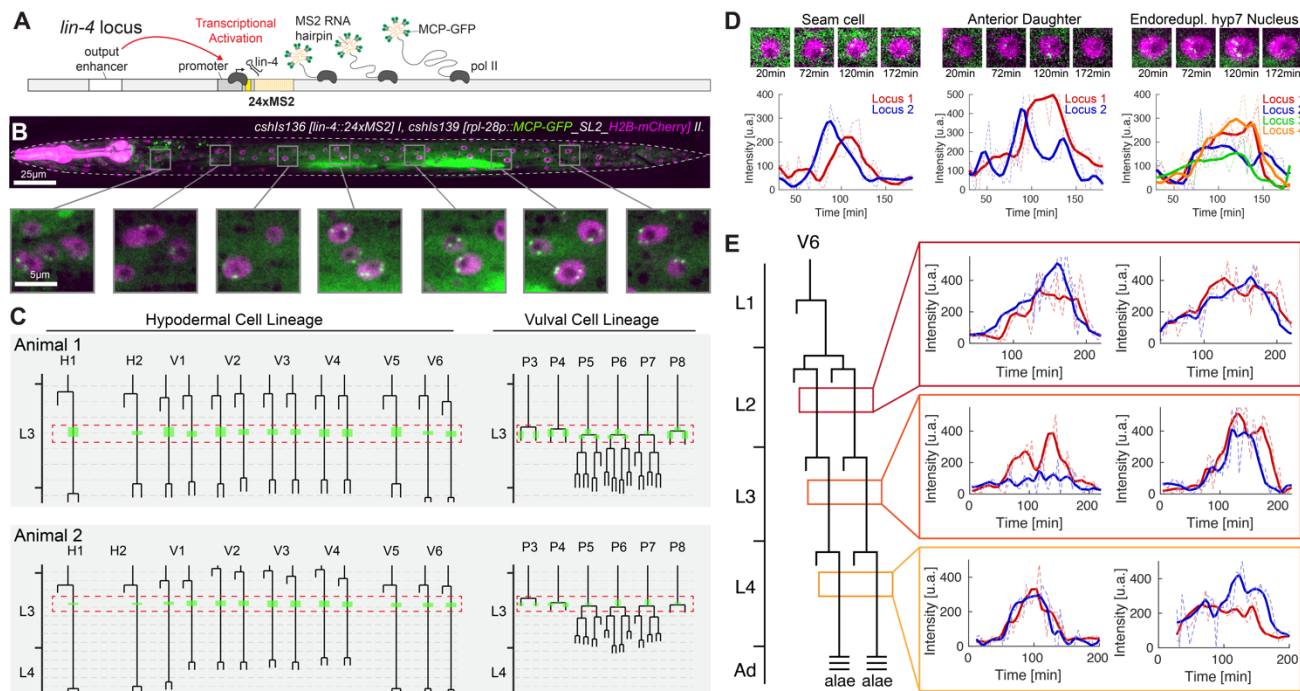
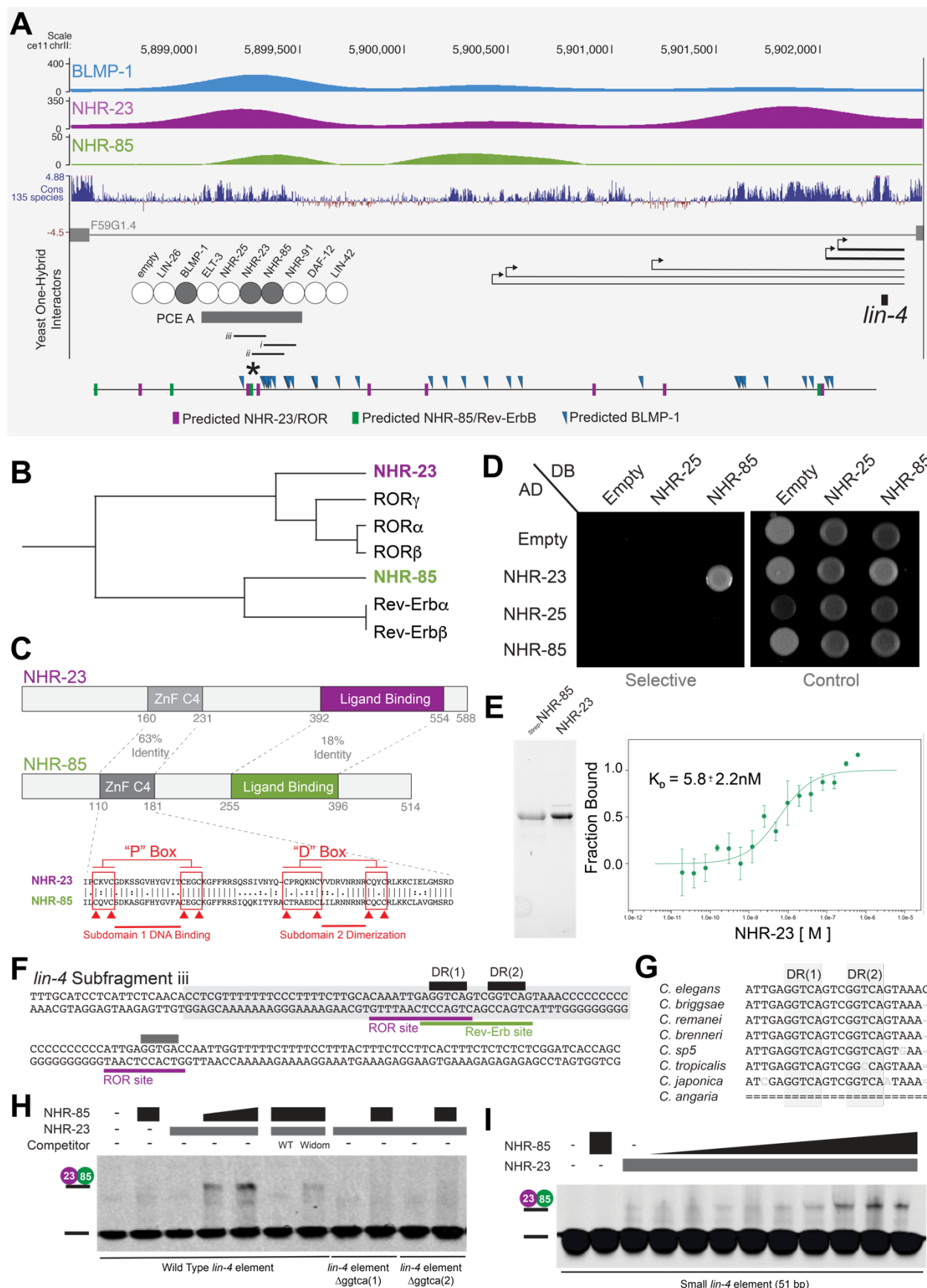


**Fig. 1. *lin-4* transcription is highly pulsatile at each larval stage.** (A) The MS2/MCP system is composed of a MS2 coat protein GFP fusion (MCP-GFP) which can bind to MS2 RNA hairpins encoded within primary miRNA transcripts. (B) Image of mid-L3 staged larva and magnified insets showing MCP-GFP spots in hypodermal cells along the anteroposterior axis. (C) Two examples of L3/L4 hypodermal and vulval precursor cell lineages, with overlaid expression patterns indicating when MCP-GFP foci were visible in each lineage. (D) Snapshots of individual seam cell and hyp7 cell expression trajectories from L3-staged animals. (E) Expression traces in pairs of V6.p seam cells from L2, L3, and L4 staged animals.



395 **Fig. 2. NHR-85<sup>Rev-Erb</sup> and NHR-23<sup>ROR</sup> form a heterodimeric complex that binds cooperatively to**  
396 **regulatory elements controlling pulsatile *lin-4* transcription. (A)** BLMP-1, NHR-85 and NHR-23  
397 bind to the *lin-4* PCE in one-hybrid assays (11). Browser tracks showing BLMP-1, NHR-23 and NHR-  
398 85 bindings sites near the *lin-4* locus. Also indicated are the major *lin-4* pri-miRNAs (21), the  
399 computationally defined binding sites for each TF, and the sub-fragments of the *lin-4* PCE element  
400 used in gel shifts below. Asterisk indicates location of the direct repeats of GGTCA in PCE element.  
401 **(B)** Sequence relationships between NHR-23 and NHR-85 and human Rev-Erb and ROR. **(C)** NHR-  
402 23<sup>ROR</sup> and NHR-85<sup>Rev-Erb</sup> domain organization highlighting similarity in DNA binding domains. **(D)**  
403 NHR-23<sup>ROR</sup> and NHR-85<sup>Rev-Erb</sup> interact with each other in two-hybrid assays. **(E)** Recombinant, purified  
404 strep-NHR-85<sup>Rev-Erb</sup> and NHR-23<sup>ROR</sup> interact in MST binding assays. **(F)** Sequences of the PCE sub-  
405 fragment iii from A and the 51bp minimal binding element (grey box) derived from *lin-4* PCEiii. **(G)**  
406 Conservation of the direct repeats DRs in the PCE elements of different nematode species. **(H and I)**  
407 EMSA experiments of wild-type and mutant target DNAs using recombinant NHR-85<sup>Rev-Erb</sup> and NHR-  
408 23<sup>ROR</sup>.  
409

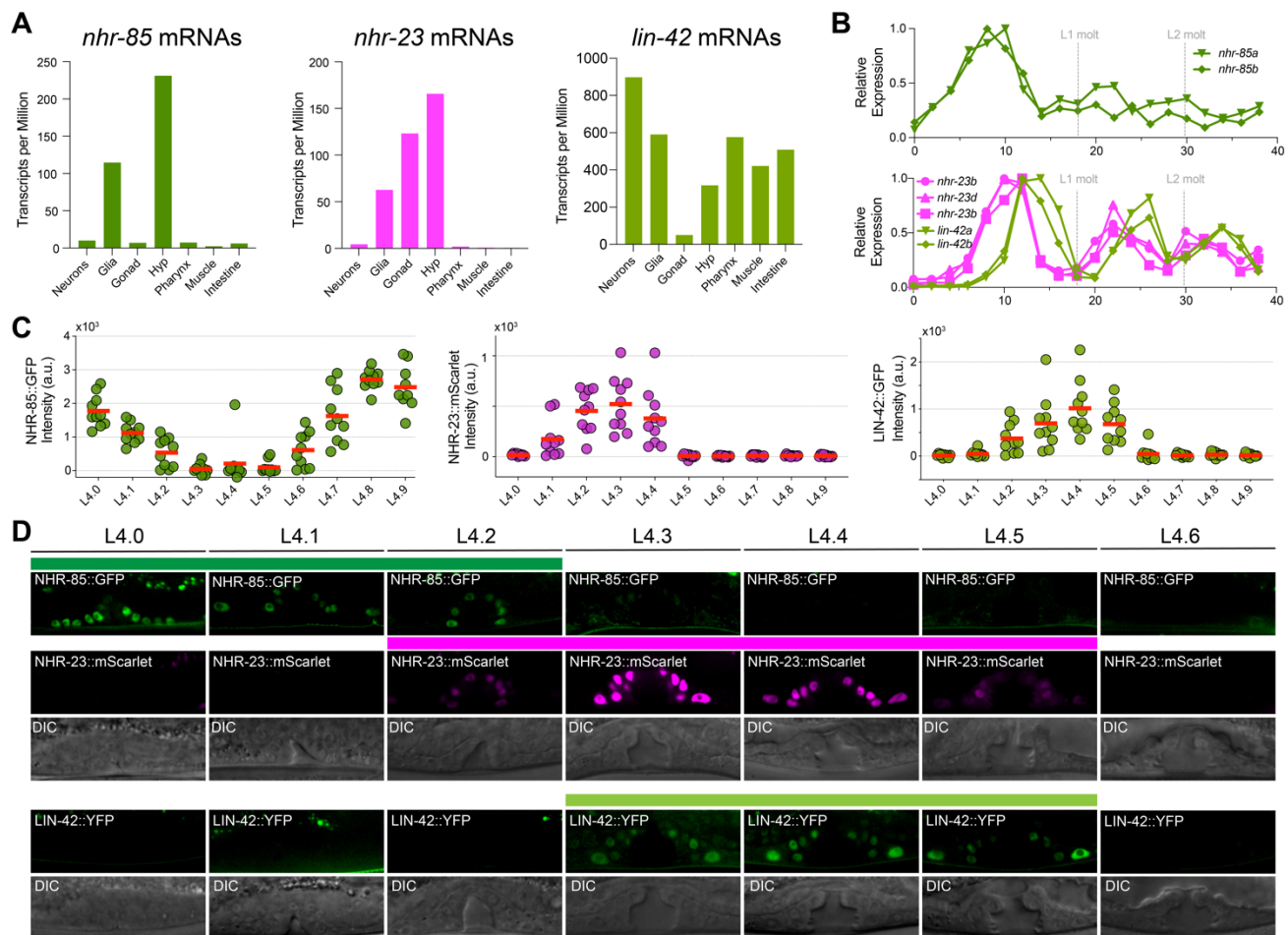


**Fig. 3. NHR-85<sup>Rev-Erb</sup>, NHR-23<sup>ROR</sup>, and LIN-42<sup>Period</sup> exhibit phased, overlapping expression patterns.** (A) Single-cell mRNA expression analysis of *nhr-85*, *nhr-23*, and *lin-42* transcripts from L2 staged animals. (B) RNA-seq time course data of *nhr-85*, *nhr-23*, and *lin-42* mRNA expression patterns. (C-D) Quantification (C) and micrographs (D) depicting NHR-85<sup>Rev-Erb</sup>::GFP, NHR-23<sup>ROR</sup>::mScarlet, and LIN-42<sup>Period</sup>::YFP expression in hypodermal seam cells and vulval cells, respectively, in each morphologically defined L4 substage (30). Circles represent individual animals (3 cells sampled); red bars indicate the mean. Colored bars indicate ranges of detectable expression.



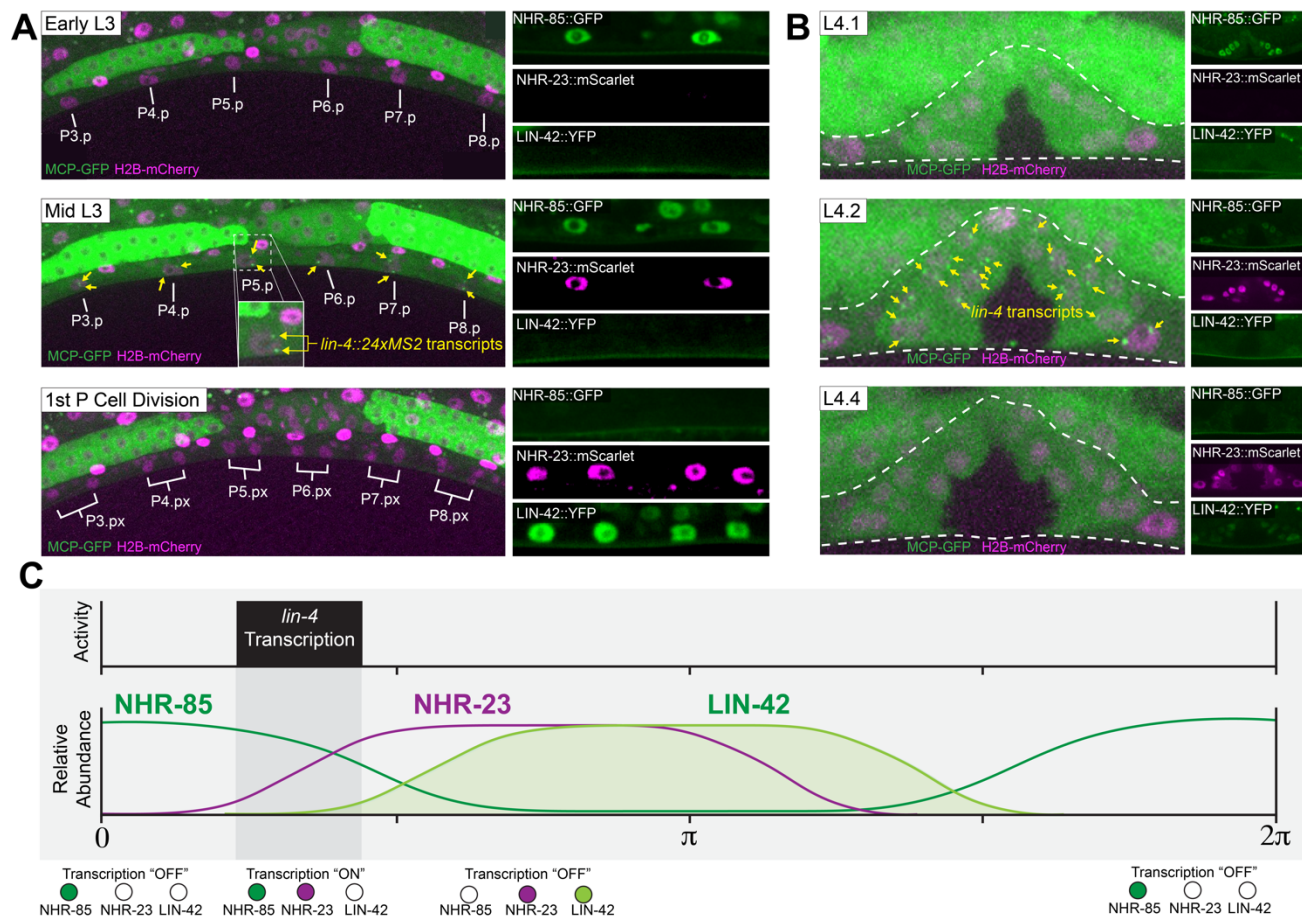


**Fig. 4. *lin-4* transcription occurs during periods where NHR-85<sup>Rev-Erb</sup>::GFP and NHR-23<sup>ROR</sup>::mScarlet are co-expressed and LIN-42<sup>Period</sup>::YFP and NHR-85<sup>Rev-Erb</sup>::GFP exhibit antiphasic expression patterns.** (A) Time course experiments of MCP-GFP demonstrate that *lin-4::24xMS2* expression occurs immediately before the first Pn.p cell divisions and not until NHR-85<sup>Rev-Erb</sup>::GFP and NHR-23<sup>ROR</sup>::mScarlet are co-expressed in the vulval precursor cells. *lin-4::24xMS2* expression terminates by the time NHR-85<sup>Rev-Erb</sup>::GFP expression is extinguished in second division VPC. The cessation of *lin-4::24xMS2* expression corresponds to time when LIN-42<sup>Period</sup>::YFP accumulates in these cells. (B) The dynamics of *lin-4::24xMS2* transcription in L4 staged vulvas. *lin-4::24xMS2* expression occurs at the same developmental stage where NHR-85<sup>Rev-Erb</sup>::GFP and NHR-23<sup>ROR</sup>::mScarlet co-expressed. As with L3-stage expression of *lin-4::24xMS2*, MCP-GFP foci are diminished around the onset time of LIN-42<sup>Period</sup>::YFP expression. (C) Image summarizing the relationship between dynamic expression patterns of NHR-85<sup>Rev-Erb</sup>, NHR-23<sup>ROR</sup>, and LIN-42<sup>Period</sup> with the period of *lin-4* transcriptional activation in the L3/L4 stages.

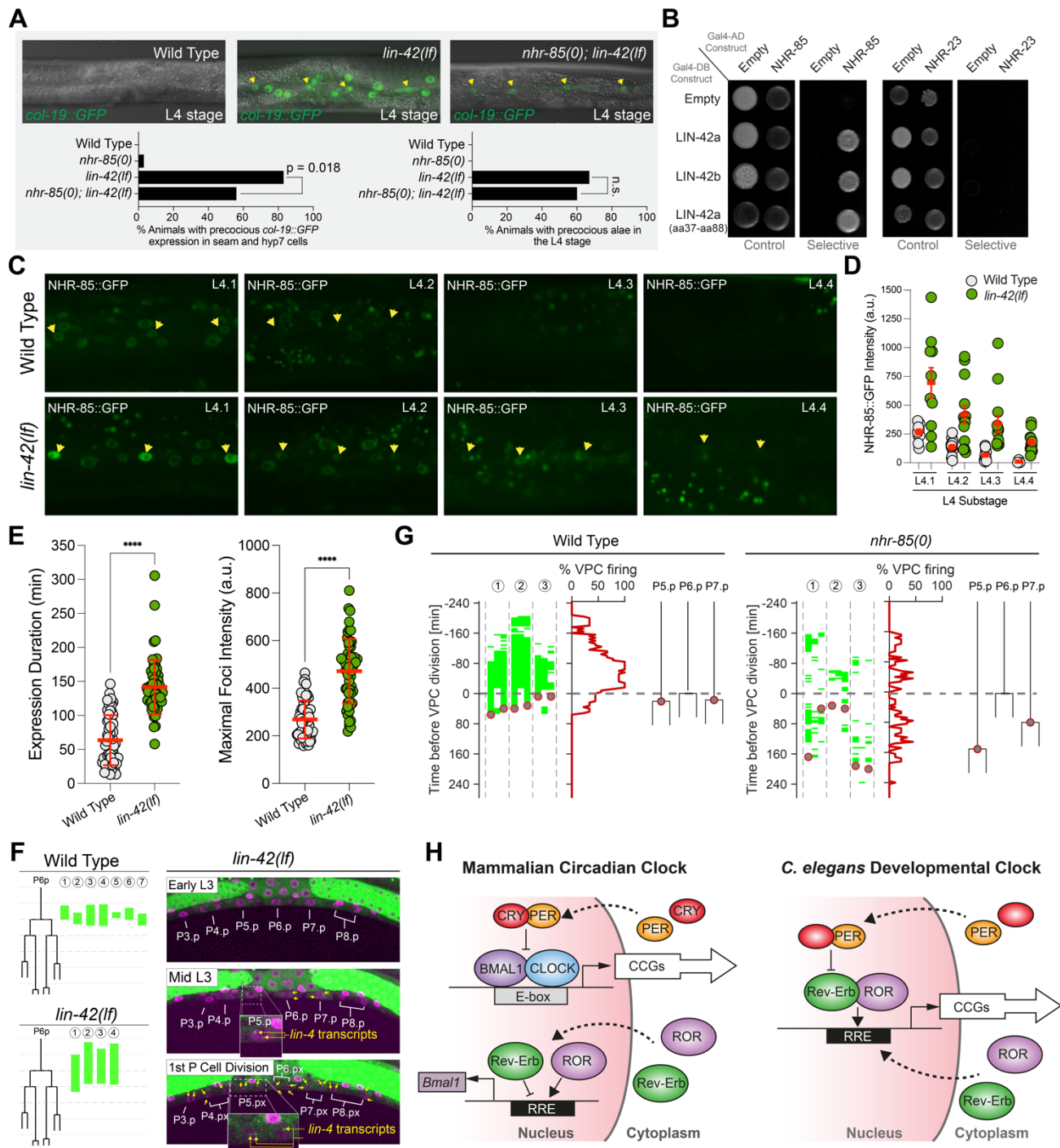


**Fig. 5. LIN-42<sup>Period</sup> binds to and regulates the expression dynamics of NHR-85 to control the amplitude and duration of *lin-4* transcription.** (A) *lin-42(lf)* mutants express *col-19::GFP* during the L3 stage of development and deletion of *nhr-85(0)* suppresses these phenotypes. Yellow arrows indicate the lateral seam cells of L4-staged animals. Error bars were calculated using two-tailed chi-square analysis. (B) LIN-42 isoforms interact with NHR-85<sup>Rev-Erb</sup> but not NHR-23<sup>ROR</sup> in two-hybrid assays. (C and D) Representative images and quantification of NHR-85<sup>Rev-Erb</sup>::GFP expression



441 dynamics in hypodermal cells of L4-staged wild-type and *lin-4(lf)* animals. Yellow arrows indicate the  
 442 lateral seam cells of L4-staged animals. Circles represent average expression in three seam cells of  
 443 an individual animal. Error bars show mean and standard deviation. Significance calculated using  
 444 Welch's t-test. **(E)** Quantification of the duration and intensity of MCP-GFP foci in L3-staged animals.  
 445 Error bars and significance calculated as in D. **(F)** Time course analysis of the onset/offset times for  
 446 MCP-GFP foci in VPCs of wild-type and *lin-42(lf)*. Green lines indicate timing of *lin-4::24xMS2*  
 447 expression in P6.p cells of individual animals. Pictographs show a representative image of the ventral  
 448 surface of a single *lin-42(lf)* animal throughout the time course. **(G)** High-resolution time course  
 449 analysis of *lin-4::24xMS2* expression in wild-type and *nhr-85(0)* mutants, aligned to first P6.p cell  
 450 division (t=0). Green areas indicate detectable MCP-GFP foci in individual P cells (P5.p – P7.p) (n =  
 451 3 animals). Grey circles represent the timing of P5.p and P7.p divisions. **(H)** Model of the mammalian  
 452 circadian clock and *C. elegans* developmental clock uncovered in this study.  
 453

## Supplemental Information to Accompany

### Circadian rhythm orthologs drive pulses of heterochronic miRNA transcription in *C. elegans*

Brian Kinney<sup>1\*</sup>, Shubham Sahu<sup>2\*</sup>, Natalia Stec<sup>1</sup>, Kelly Hills-Muckey<sup>1</sup>, Dexter W. Adams<sup>3,4</sup>, Jing Wang<sup>1</sup>, Matt Jaremako<sup>3</sup>, Leemor Joshua-Tor<sup>3</sup>, Wolfgang Keil<sup>2,†</sup>, Christopher M. Hammell<sup>1,†</sup>

<sup>1</sup>Cold Spring Harbor Laboratory, Cold Spring Harbor, NY 11724, USA.

<sup>2</sup>Institut Curie, Université PSL, Sorbonne Université, CNRS UMR168 Laboratoire Physico Chimie Curie, 75005 Paris, France.

<sup>3</sup>Howard Hughes Medical Institute, W. M. Keck Structural Biology Laboratory, Cold Spring Harbor Laboratory, Cold Spring Harbor, NY, 11724, USA

<sup>4</sup>Graduate Program in Genetics, Stony Brook University; Stony Brook, NY 11794, USA

\*These authors contributed equally

<sup>†</sup>Correspondence: wolfgang.keil@curie.fr (W.K.); chammell@cshl.edu (C.M.H.) (lead contact)

# SUPPLEMENTAL FIGURES:

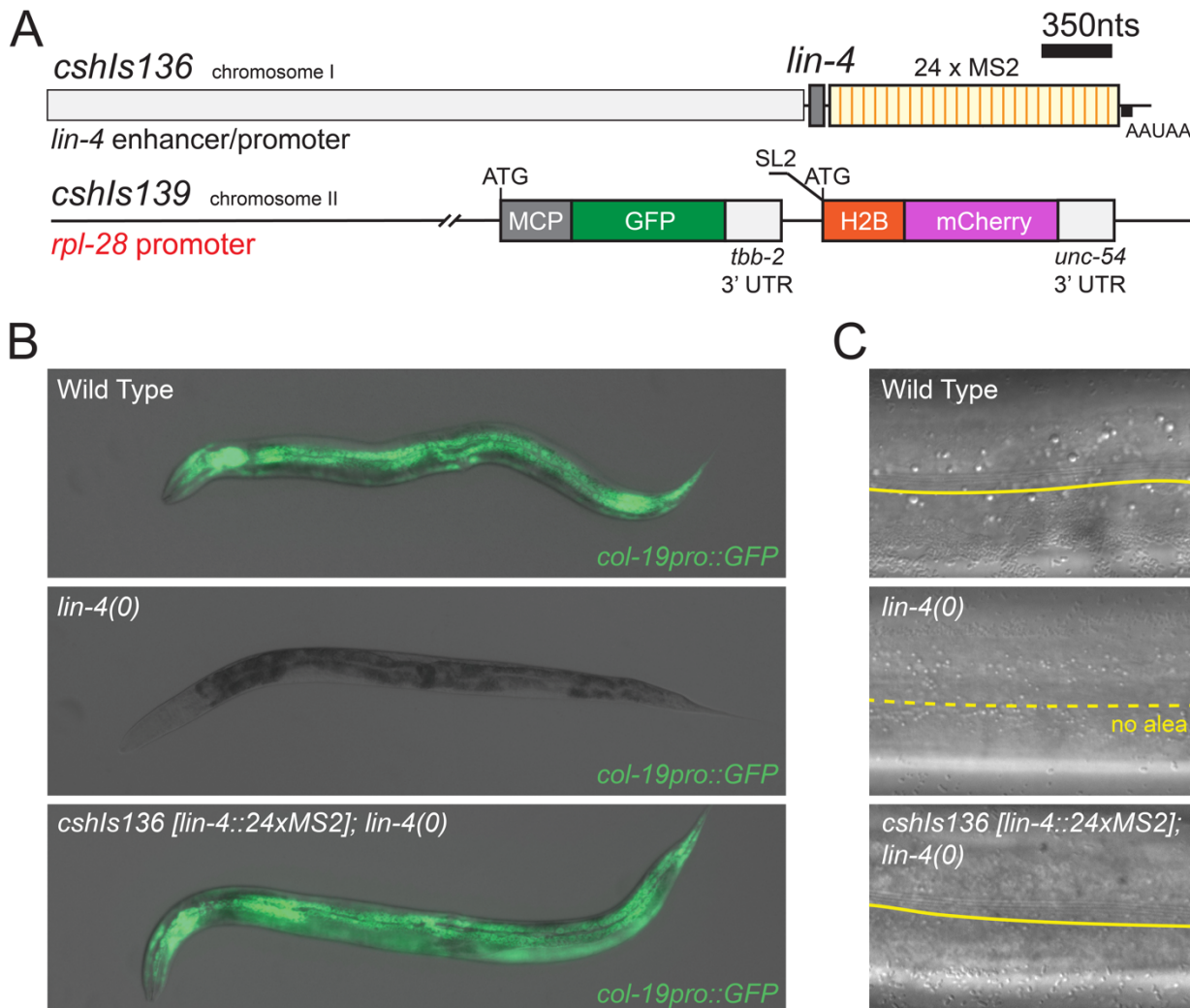


**Fig. S1. The single copy, MS2-tagged *lin-4* transgene rescues *lin-4* temporal patterning defects.** (A) Wild-type animals express a *col-19::GFP* transgene immediately after the L4 molt (100%; n = 50) while *lin-4(e912)* mutants fail to induce *col-19::GFP* expression (0% expressing; n = 43). *cshIs136 [lin-4::24xMS2; unc-119(+)* I; *lin-4(e912)* I] animals exhibit normal *col-19::GFP* expression (100% expressing; n = 30). (B) Wild-type animals generate adult-specific alae structures on the cuticles of young adult animals (100%; n = 23). 100% (n = 40) of *lin-4(e912)* animals lack these structures. *cshIs136 [lin-4::24xMS2; unc-119(+)* I; *lin-4(e912)* I] animals exhibit wild-type adult alae (100%; n = 40).

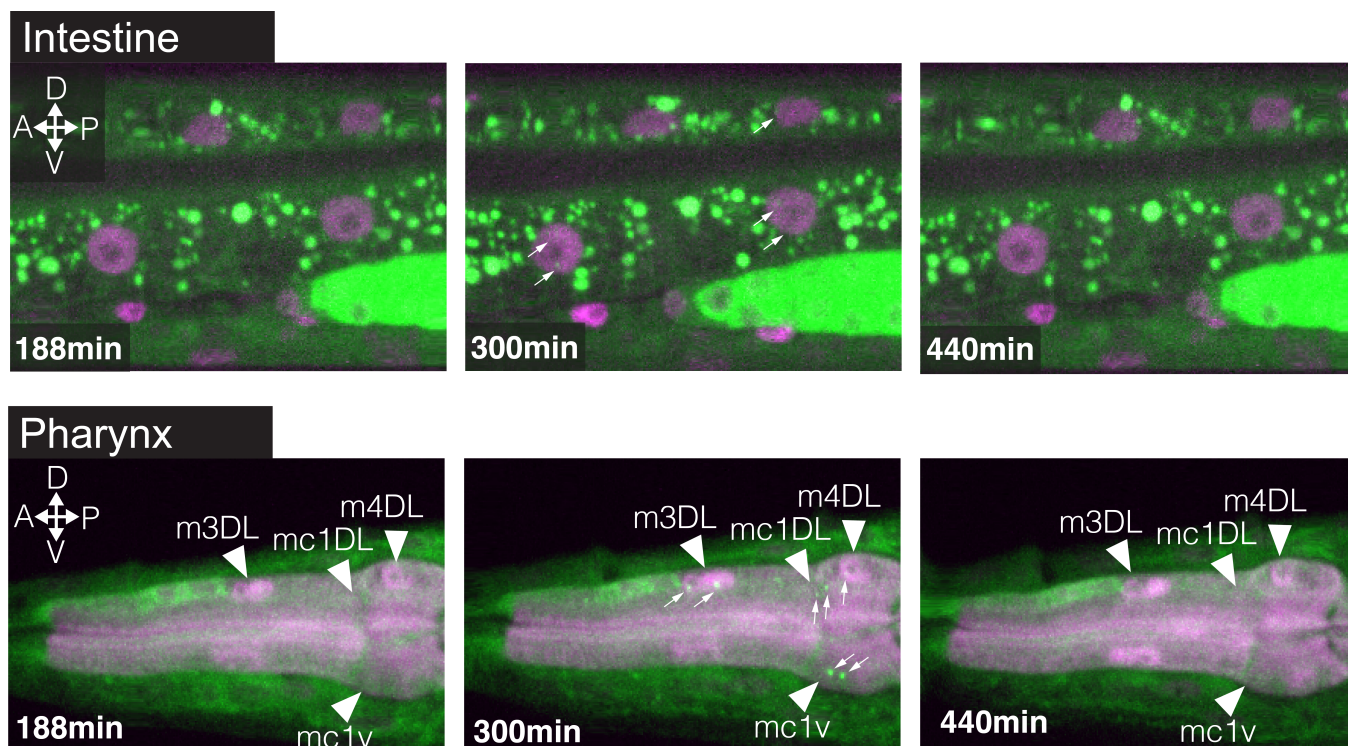


**Fig. S2. *lin-4::24xMS2* expression is pulsatile in other somatic cells.** Timeseries of *lin-4::24xMS2* expression in intestine cells and cells of the pharynx in L3-staged animals. Small arrows indicate MCP-GFP foci and triangles indicate the location of the indicated cell.

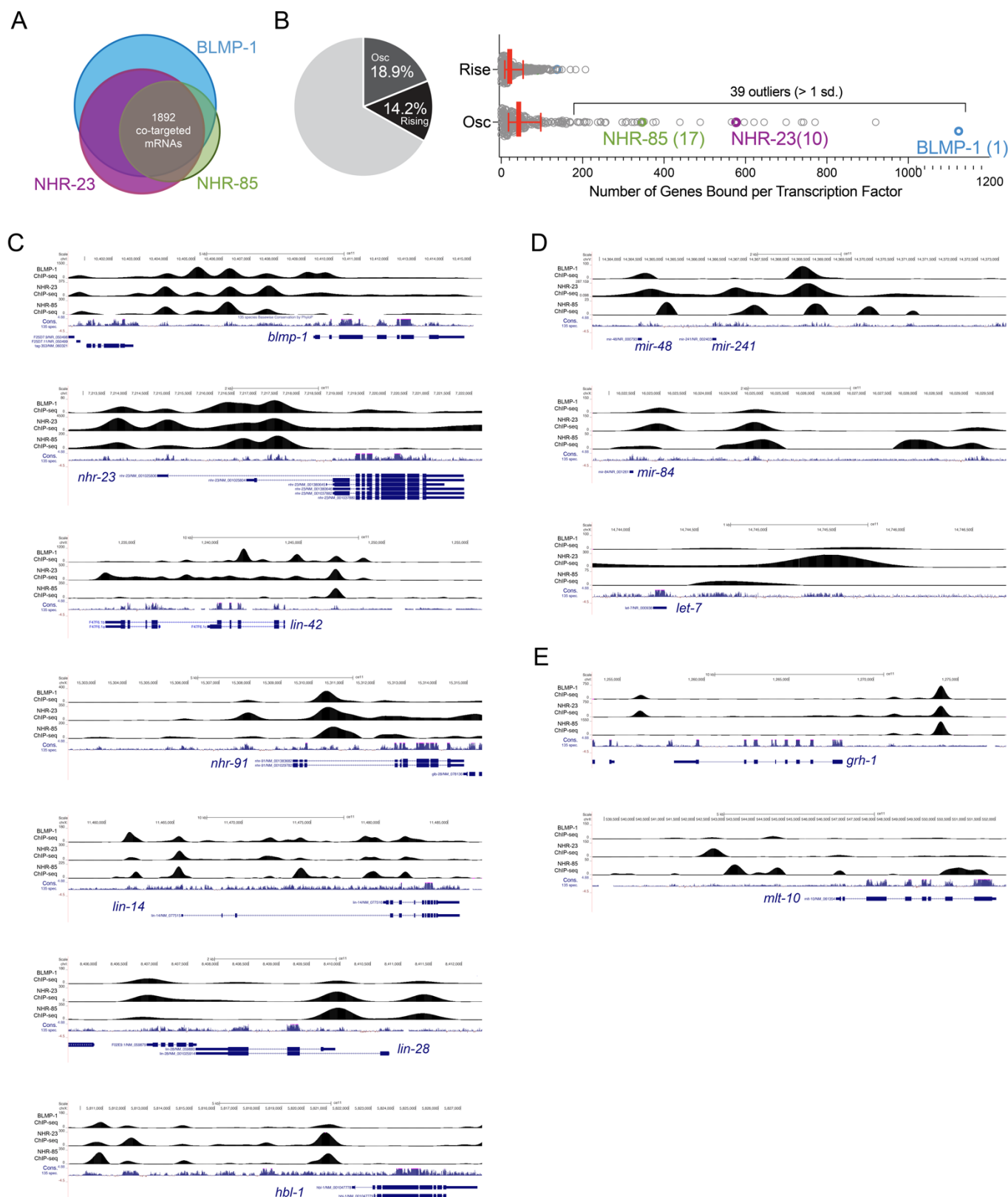


**Fig. S3. BLMP-1, NHR-23<sup>ROR</sup>, and NHR-85<sup>Rev-Erb</sup> binding sites are enriched in the promoters of cyclically transcribed genes as well as genes that function in the heterochronic pathway. (A)**

493 Venn diagram indicating the level of overlap of genes targeted by BLMP-1, NHR-85 and NHR-23.  
 494 For this analysis, peaks from NHR-85<sup>Rev-Erb</sup>, NHR-23<sup>ROR</sup> and BLMP-1 ChIP-seq experiments were  
 495 assigned to the nearest proximal protein coding genes (+3kb upstream and 300bp downstream)  
 496 (Tables S1 and S2). (B) NHR-85<sup>Rev-Erb</sup>, NHR-23<sup>ROR</sup> and BLMP-1 binding sites are enriched in the  
 497 promoters of genes that exhibit oscillatory expression patterns. Calculations were derived from  
 498 population-based RNA-seq time course data sets (8) that partition the expression of post-  
 499 embryonically expressed genes into three types: (i) transcripts with their transcriptional periodicity  
 500 tied to the molting cycle (osc; 18.9%; 2,718 of 14,378 total genes) (ii) genes with rising expression  
 501 throughout larval development (rising; 14.2%) and (iii) genes with flat expression profile (flat; 66.9%)  
 502 (Fig. 2E). Using these data sets, we compared the numbers of cyclically expressed genes that were  
 503 targeted by NHR-85<sup>Rev-Erb</sup> or NHR-23<sup>ROR</sup> to those targeted by any of the other 170 TFs queried in by  
 504 the *C. elegans* ModEncode Project (using 265 publicly available, validated ModEncode ChIP-seq  
 505 data-sets (tables S1 and S2)(48). (C) Browser tracks overlaying the BLMP-1, NHR-23<sup>ROR</sup>, and NHR-  
 506 85<sup>Rev-Erb</sup> ChIP-seq signal near the indicated loci.

507



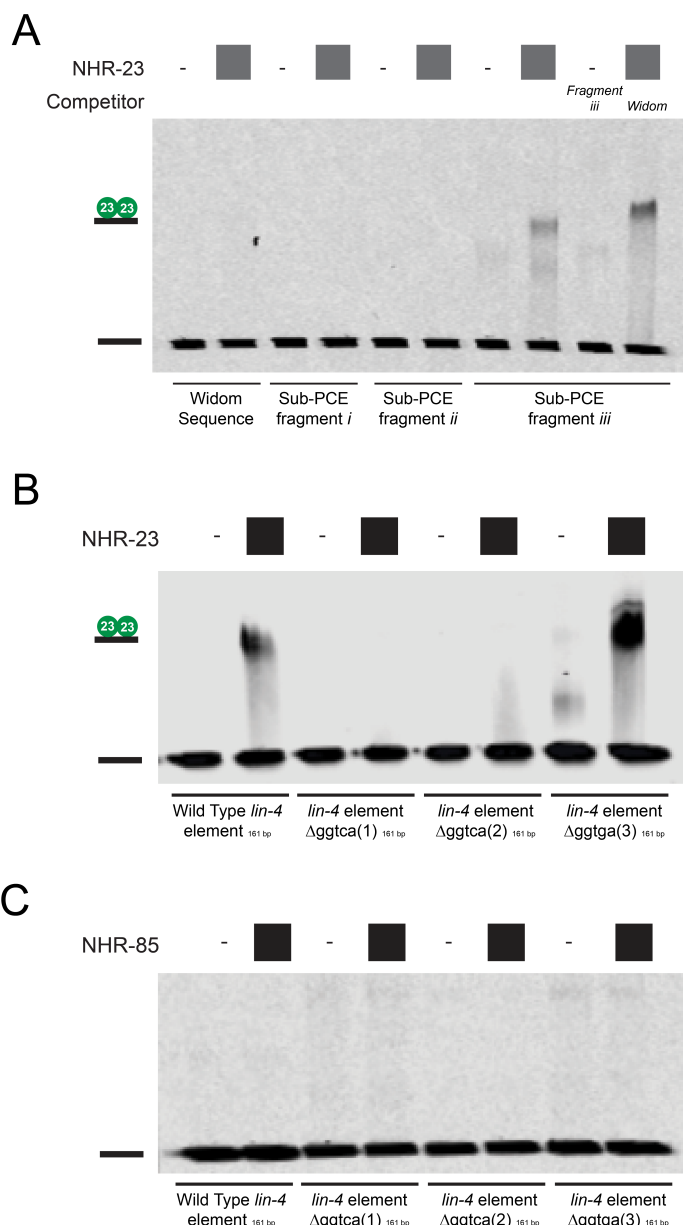


**Fig. S4. NHR-23<sup>ROR</sup> can bind the *lin-4* sub-fragment III at high protein concentrations while NHR-85<sup>Rev-Erb</sup> cannot.** (A) NHR-23<sup>ROR</sup> can bind specifically to PCE sub-fragment III that contains both direct repeats outlined in Fig. 2F and G. (B) NHR-23<sup>ROR</sup> binding to the PCE sub-fragment III requires the two direct repeats but does not require the un-conserved single GGTGA element downstream of the direct repeats (see Fig. 2 for details). (C) NHR-85<sup>Rev-Erb</sup> does not bind to any of the PCE sub-elements to any appreciable degree.

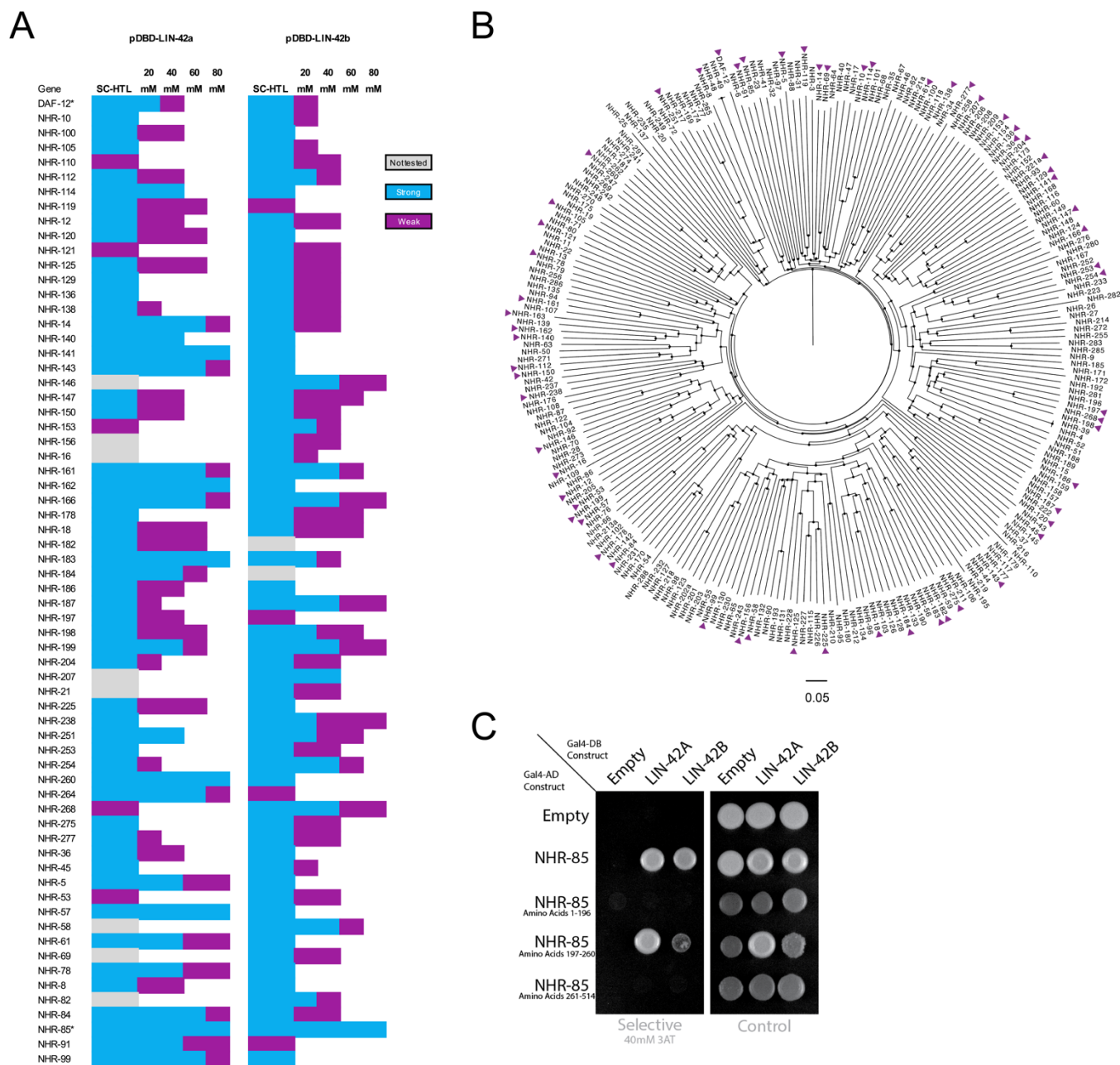


**Fig. S5. LIN-42<sup>Period</sup> interacts with multiple *C. elegans* NHRs and interacts with NHR-85<sup>Rev-Erb</sup> via the hinge region that separates the DNA-binding domain and ligand-binding domain. (A)** A list depicting the NHRs that interact with one of the two two-hybrid baits for LIN-42 (LIN-42a and LIN-42b isoforms). Colors indicate the level of yeast growth solid growth media containing the indicated concentration of 3-AT. **(B)** Dendrogram of *C. elegans* nuclear hormone receptors showing the relationships between conserved sub-families of NHRs and the distribution of LIN-42 interactions within this large family of TFs. Purple triangles indicate NHRs that interact with one or both LIN-42



524 isoforms. **(C)** Two hybrid results that indicate that both LIN-42 isoforms can interact with the central  
 525 hinge region of NHR-85.

526

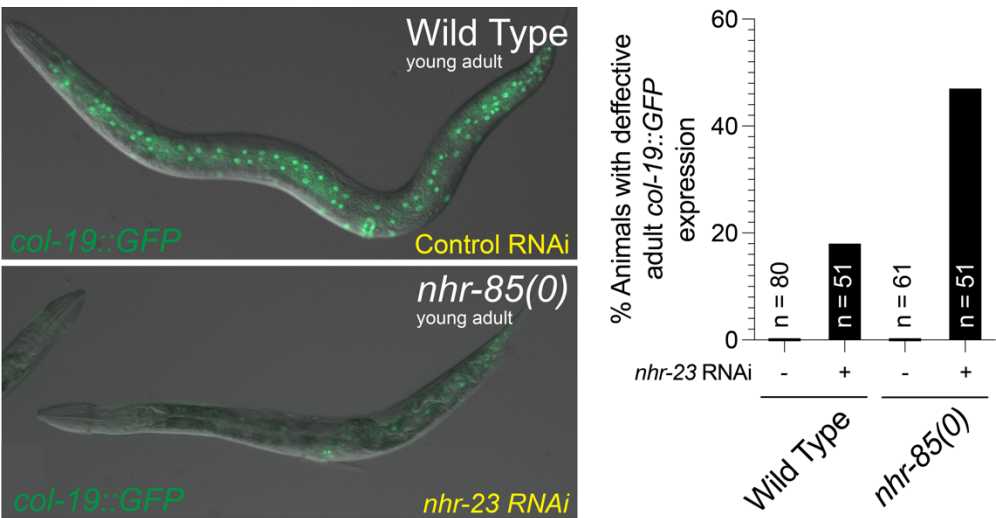


**Fig. S6. Depletion of *nhr-23* results in defects in expressing adult-specific GFP reporters after the L4 molt.** The adult-specific *col-19::GFP* reporter is expressed in both seam and hyp7 cells in wild-type animals. Depletion of *nhr-23* prevents normal expression of *col-19::GFP* during adulthood. In *nhr-23* RNAi treated animals, the indicated percentage of animals expressed *col-19::GFP* in the head and tail cells of the hypodermis. The reduction of *col-19::GFP* expression in young adult animals is stronger in animals lacking *nhr-85*. *nhr-23* RNAi cultures were diluted to 50% with control RNAi bacteria to enable animals to develop to adulthood and avoid the fully penetrant larval arrest phenotypes associated with undiluted *nhr-23* RNAi cultures.

## MATERIALS AND METHODS:

**C. elegans maintenance and genetics.** *C. elegans* strains were maintained on standard media at 20°C and fed *E. coli* OP50 (49). Some strains were provided by the CGC, which is funded by NIH Office of Research Infrastructure Programs (P40 OD010440). A complete list of strains is outlined in Table S3.

**RNAi Feeding.** RNAi by feeding was performed using *E. coli* HT115 expressing double stranded RNA corresponding to the indicated target gene or containing a control dsRNA expression plasmid that does not contain sequences corresponding to any *C. elegans* gene (50, 51). To prevent contamination by *E. coli* OP50, L4-staged animals were added to RNAi plates individually after removing co-transferred bacteria. For RNAi against *nhr-23*, bacterial cultures were diluted with control RNAi cultures at the indicated levels prior to experimental onset. In experiments in Fig. S6, starved L1 animals of the indicated genotypes were used. Unless otherwise noted, F1 progeny were analyzed for RNAi-induced phenotypes in the following 2-4 days. Plasmids used for RNAi are outlined in Table S4.

**CRISPR genome editing.** Genome editing and transgene insertion was accomplished using standard CRISPR/Cas9-mediated genomic editing to the ttTi5605 or ttTi4348 landing site following standard protocols (52). For CRISPR/Cas9 editing of the endogenous *lin-42* gene, pCMH1434 (expressing Cas9 and a synthetic CRISPR guide RNA targeting a genomic region encoding the LIN-42 C-terminus) and pCMH1439 (encoding a LIN-42::YFP fragment) were injected in to N2 animals and screened by PCR to identify transgene insertion at the *lin-42* gene. Plasmids used to generate CRISPR alleles are outlined in Table S4.

**Microfluidics and long-term imaging.** For microfluidics experiments, early to mid L1-staged animals were isolated 6h after starvation-induced L1 arrest at 20°C before an experimental time course. Other stages were individually isolated by observing defined cellular and morphological features indicative of animals developmental stage (1). Animals were mounted into the microfluidic device as previously described (22). During the imaging process, animals were constantly fed NA22 *E. coli* suspended in S medium. The temperature was kept constant at 20°C both, at the objective and the microfluidic device using a custom-built water-cooled aluminum ring (for objective) and custom-built aluminum stage inset that was directly coupled to a thermal Peltier device.

575

576 **Image acquisition.** MS2-MCP-GFP live imaging Live imaging was performed with a 60x, 1.2NA  
577 objective on a Nikon Ti2 Eclipse microscope equipped with a V3 CREST spinning disk confocal  
578 module. To ensure fast multichannel acquisition, hardware triggering was implemented between a  
579 MadCityLabs NANO Z200-N piezo z-stage, a Photometrics Prime 95B sCMOS camera with 25mm  
580 field of view (2048x2048 pixels, pixel size 11um corresponding to 183nm), and a Lumencor® Celesta  
581 solid-state laser source via a National Instruments (NI) PCIe-6323 card. Laser wavelengths of 488nm  
582 and 545nm were used to excite MCP-GFP and histone-mCherry, respectively. Acquiring a dual-color  
583 z-stack with 51 slices and 50ms exposure times takes approximately 3.2 seconds with this setup.

584

585 Confocal Microscopy: Images were acquired using a Hamamatsu Orca EM-CCD camera and a  
586 Borealis-modified Yokagawa CSU-10 spinning disk confocal microscope (Nobska Imaging, Inc.) with  
587 a Plan-APOCHROMAT x 100/1.4 or 40/1.4 oil DIC objective controlled by MetaMorph software  
588 (version: 7.8.12.0). Animals were anesthetized on 5% agarose pads containing 10mM sodium azide  
589 and secured with a coverslip. Imaging on the microfluidic device was performed on a Zeiss AXIO  
590 Observer.Z7 inverted microscope using a 40X glycerol immersion objective and DIC and GFP filters  
591 controlled by ZEN software (version 2.5). Images were captured using a Hamamatsu C11440 digital  
592 camera. For scoring plate level phenotypes, images were acquired using a Moticam CMOS (Motic)  
593 camera attached to a Zeiss dissecting microscope.

594

595 Wide-field Fluorescence microscopy:

596 Images were acquired with a Zeiss Axio Observer microscope equipped with Nomarski and  
597 fluorescence optics as well as a Hamamatsu Orca Flash 4.0 FL Plus camera. An LED lamp emitting  
598 at 470 nm was used for fluorophore excitation. For single images, animals were immobilized on 2%  
599 agarose pads supplemented with 100mM Levamisole (Sigma). For single images, animals were  
600 immobilized on 2% agarose pads supplemented with 100mM Levamisole (Sigma). For long-term  
601 imaging methods, see Microfluidics and Long-term Imaging section.

602

603 **Fluorescent Reporter Quantification.** Reporter lines were imaged using wide-field fluorescence or  
604 confocal microscopy as described above. The average intensity (arbitrary unites) per seam cell was  
605 measured using ImageJ. Each seam cell intensity was determined by the measurement of fluorescent

intensity of the nucleus minus the intensity of a background sample. The fluorescent intensity of each animal was determined by the average of three seam cells. Ten animals per developmental stage were imaged unless otherwise noted.

## **MCP-GFP live imaging.**

Long term imaging: For long-term live imaging across several larval stages, animals were mounted in a microfluidic chamber 6h after L1 arrest and grown on NA22 bacteria suspended in S-medium until mid L4 as previously described (22). At each time point, animals were *reversibly* immobilized using microfluidic pressures and flows. A z-stack of 51 images separated by 0.5um was acquired at four overlapping positions, covering the entire microfluidic chamber. Thereafter, the animal was released from immobilization and left to roam and feed freely until the next time point.

Short term imaging: For short-term live imaging (Figs. 1, 4 & 5) developmentally staged animals were mounted into the microfluidic chamber as previously described (22), a few hours before the expected appearance of MS2 spots. Minutes before the appearance of MS2 spots, animals were immobilized using microfluidic pressures and flows and kept immobilized for the entire duration of the experiment. This allowed to maintain a stable worm position enabling automated analyses (see below). At each time point (every 4min), a stack of 21 images separated by 0.5um was acquired at four overlapping positions, covering the entire microfluidic chamber. Occasionally, animals arrested development upon prolonged immobilizations, as evident by the cessation of germ line divisions (L2-L4 larvae), the cell-cycle arrest of vulval precursor cells (VCPs) (L3 larvae) or by failure to advance through vulval morphogenesis (L4 larvae). These animals were excluded from further analysis. As opposed to all other genotypes imaged, *nhr-85(0)* mutants animals exhibited a pronounced tendency to roll under these imaging conditions, precluding MS2 spot tracking within nuclei of the lateral hypodermis.

## **MCP-GFP live imaging data analysis.**

### Short term imaging:

All events (cell divisions, onset and offset of MCP-GFP spots) were scored manually in the time series. For short-term live imaging, all analysis was performed using custom-written FIJI macros, pixel classification with random forest trees in Ilastik and MATLAB® scripts. The main challenge in

this analysis is residual animal movement between time points as well as low signal-to-noise ratio of the MCP-GFP signal.

### Long term imaging and 3D tracking:

First, the worm backbone was detected in each frame by skeletonization, using a thresholded probability map, obtained by processing a maximum z-projection of the MCP-GFP channel, through a custom-trained Ilastik pixel classifier. Next, computational straightening was performed along this backbone (22) to obtain a time series of straightened worm z-stacks. This straightened time series has the advantage that residual movement is primarily along the anteroposterior animal axis. Next, we divided the straightened worm z-stack along the worm axis into overlapping (20%) segments of 500 pixels (~91um) in length. Each of these segments was then manually registered to obtain z-stacks in which tracking of almost all hypodermal nuclei could automatically performed with minimal user corrections. To improve nuclear signal for segmentation, the histone-mCherry signal was augmented, using a custom-trained Ilastik pixel classifier. 3D tracking and manual correction was then performed on the resulting Ilastik probability maps using the FIJI TrackMate plugin (53) with LoG detector and LAP tracker. For each segment, frames with substantial animal movement *between* z-slices were excluded from subsequent analysis. Whenever nuclei were tracked twice (due to overlapping worm segments), the nucleus with the most tracked time points was chosen for subsequent MCP-GFP spot analysis.

**MCP-GFP spot tracking and intensity quantification.** MS2 spots were tracked in each tracked nucleus, using the FIJI TrackMate plugin with LoG detector and LAP tracker and the Ilastik nucleus probability maps as mask to include only spots inside nuclei. Each MCP-GFP spot track was manually corrected, and spots were added to frames occasionally, in which the TrackMate LoG detector failed to detect them. For quantification of MCP-GFP spot intensities, a 2D Gaussian fit to the maximum z-projection of three z-slices around the peak slice determines the position of the spot. Background was calculated as the average intensity in a ring between 3 and 5 pixels away from the spot position. The spot intensity was calculated by integrating the fluorescence over a circle with a radius of 2 pixels around the spot position and subtracting the estimated background.

**MS2-MCP-GFP trace analysis.** MCP-GFP traces were smoothed with a Gaussian of width 1.5 frames (6 minutes). Using this filtered trace, for each tracked locus, duration and maximum intensity

during the transcriptional pulse was determined. Loci were considered “ON”, if spot intensity was above 150 counts and “OFF” if below. Duration of transcription for each locus was determined as the time interval between the first “ON” time point and the last. Typically, loci stayed “ON” for the entire duration of the transcriptional pulse within a given larval stage.

**Yeast two-hybrid.** Plasmids containing target proteins fused to GAL4 DNA-binding-domain (pDBD) and GAL-4 Activation Domain (pAD) were co-transformed into the pJ69-4a Y2H yeast strain (54) as previously described (55, 56). Transformed yeast was plated on SC-TRP-LEU plates for three days. Three colonies from each transformation plate were streaked onto SC-HIS-TRP-LEU plates containing 3-AT at the indicted concentrations. Protein interactions were determined by visible growth on 3-AT conditions with negative growth in empty vector controls after three days. For the large-scale LIN-42 screen, pDBD containing LIN-42a, LIN-42b, and the empty vector control were individually mated to each pAD construct from the WTF2.2 yeast library (Reece-Hoyes et al., 2011) (57). For visualization of results, individual colonies were grown overnight in YPD in 96-well plates. Overnight cultures were diluted 1/200 in ddH<sub>2</sub>O and 3μL was pipetted on to selective 3-AT and control plates. After three days of growth, plates were imaged on a Fotodyne FOTO/Analyst Investigator/FX darkroom imaging station. Plasmids used in 1- and 2-hybrid experiments are outlined in Table S4.

**Bioinformatic analysis of BLMP-1, NHR-82, and NHR-23 ChIP-seq data.** ChIP-seq short reads were first clipped off adaptor sequences. Reads of minimum 22bp were mapped to the UCSC *C. elegans* genome (ce10) using bowtie program<sup>76</sup> (58) looking for unique alignments with no more than 2 mismatches. MACS program (v1.4)(59) was used for peak calling with significant p-value cutoff equals 1e-5. Target annotations were based on WormBase (version 220) using customized R scripts and Bioconductor packages. ModeEncode data sets (48) (BLMP-1(ENCF108AEB and ENCF1615AMZ), NHR-23(ENCF1019QMH) and NHR-85(ENCF1018KHA)) were used in the initial analysis and we defined the promoter region as upstream 3kbp to downstream 300bp around the transcription start site (TSS). Peaks located in promoter regions were annotated to their closest TSS sites for both coding and non-coding genes (Table S1). These potential targets were then overlapped to sets of oscillatory genes identified in a previous mRNA-seq-based study (8). Overlapping target gene sets organized in Figure 2D are from postembryonic ChIP-seq samples for each TF. Raw data for each of the 265 ModEncode data sets (annotation numbers listed individually in Table S1) used in Figure 2E were downloaded from modENCODE (48) and processed in the same way as BLMP-1, NHR-23 and NHR-85 datasets (11). ModEncode-derived peaks from each TF ChIP-seq dataset were



compared to identify common sites with at least one base pair overlapping using BEDTools. All ChIP-seq mapping graphs and images were produced in R by customized scripts.

**Protein preparation.** Full-length *C. elegans* protein NHR-23 was cloned as a N-terminal Strep-SUMO fusion protein in a pFL vector of the MultiBac Baculovirus expression system to create pCMH1662 (60). This construct was expressed in insect Sf9 cells grown in CCM3 media (HyClone) at 27°C for 60 h. Cells were harvested by spinning at 2200 rpm for 20 min and resuspended in lysis/wash buffer (20 mM Tris pH 8.0, 200 mM NaCl, 5 mM BME) and a protease inhibitor cocktail before flash freezing in liquid N<sub>2</sub>. Cell pellets were stored at -80°C. Cell pellets were thawed and sonicated once. Poly-ethylene imine (PEI) was added at 0.2% to the lysate after cell pellets were thawed and sonicated. The lysate was then spun by ultracentrifuge at 38,000 rpm for 45 min, at 4°C. The supernatant of the lysate was then used for batch binding with Strep-Tactin superflow resin (IBA) for 1 hour while on a rolling shaker at 4°C. The affinity beads were harvested by spinning at 1000 rcf for 5 minutes, then resuspended in lysis/wash buffer and applied to a gravity column. The column was washed with 30 column volumes of lysis/wash buffer and 5 column volumes of ATP wash buffer (20 mM Tris pH 8.0, 200 mM NaCl, 5 mM BME, 2 mM ATP). The protein was eluted from the affinity column in 2 column volumes of elution buffer (20 mM Tris pH 8.0, 200 mM NaCl, 5 mM BME, 2 mM desthiobiotin). The Strep-SUMO tag was cleaved from NHR23 by ULP1\* protease overnight at 4°C. The protein was then concentrated and loaded onto a 10/300 Superdex200 Increase gel filtration column (Cytiva Life Sciences), running in lysis/wash buffer, chromatographed for ~30 mL at 0.6 mL min<sup>-1</sup>. Protein purity and cleavage efficiency was assessed by SDS-PAGE. Plasmids used to express recombinant proteins are outlined in Table S4.

Full length *C. elegans* protein NHR-85 was cloned as a N-terminal Strep-fusion protein in a pFL vector of the MultiBac Baculovirus expression system to create pCMH2206. NHR-85 was purified using the same method as above, with the exception of the overnight N-terminal tag cleavage step.

**Microscale thermophoresis analysis.** Binding assays of purified NHR23 or strep-NHR85 was measured using a Monolith NT.115 Pico running MO Control version 1.6 (NanoTemper Technologies). Assays were performed in 100 mM NaCl, 20 mM Tris pH 8.0, 0.05% Tween-20. AlexaFluor647 NHS Ester (ThermoFisher Scientific) labeled NHR-23 (200 pM) was mixed with 16 serial dilutions of strep-NHR-85 starting at 31.5 uM and loaded into microscale thermophoresis



733 premium coated capillaries (NanoTemper Technologies). MST measurements were recorded at 25°C  
734 using 30% excitation power and 60% MST power. Measurements were performed in duplicate.  
735 Determination of the binding constant was performed using MO Affinity Analysis v.2.3.

736

737 AlexaFluor647 NHS Ester (ThermoFisher Scientific) labeled strep-NHR-85 (400 pM) was mixed with  
738 16 serial dilutions of NHR-23 starting at 625 nM. MST measurements were recorded at 25°C using  
739 15% excitation power and 40% MST power. Measurements were performed in triplicate.  
740 Determination of the binding constant was performed using MO Affinity Analysis v.2.3.

741 **Gel Shifts.** For gel shifts with free DNA, 5' IRDye (IRDye700 or IRDye800)-labeled and unlabeled  
742 oligos were obtained from IDT (Coralville, Iowa) and used to amplify DNA probes of the indicated  
743 sequences. For wild-type probes, the indicated PCE fragments were amplified pCMH1954. For  
744 mutants probes that harbor mutations in either of the GGTC repeats, synthetic DNAs were obtained  
745 from Synbio Technologies (Manmouth Junction, NJ, USA) and used to amplify the corresponding  
746 mutant DNA fragments with the following sequences (mutations underlined and italicized):

747 C\_ROR(1)REV:TTTGCATCCTCATTCTCAACACCTCGTTTTTTTCCCTTTTCTTGACAAATTGAcc  
748 tgtGTCGGTCAGTAAACCCCCCCCCCCCCCCCCCATTGAGGTGACCAATTGGTTTTTCTTTTCC  
749 TTTACTTTCTCCTTCACTTTCTCTCTC TCGGATCACCAGC

750 C\_REV:TTTGCATCCTCATTCTCAACACCTCGTTTTTTTCCCTTTTCTTGACAAATTGAGGTCAG  
751 TCcctgtcTAAACCCCCCCCCCCCCCCCCCATTGAGGTGACCAATTGGTTTTTCTTTTCCTTTAC  
752 TTTCTCCTTCACTTTCTCTCTC TCGGATCACCAGC

753 For binding reactions, recombinant proteins were incubated with gel purified DNA probes in 10 mM  
754 Tris pH 7.5, 50 mM KCl, 1 mM DTT, 0.1mg/mL poly (dIdC) (Sigma-Aldrich), and 0.25% Tween 20  
755 for 30 minutes at 20°C (in dark chamber). Samples were then run in a 4% native polyacrylamide gel  
756 containing 50mM Tris pH 7.5, 0.38 M glycine and 2mM EDTA in 1x TBE buffer. Gels were imaged  
757 and quantified using a Li-Cor Odyssey Imager (Lincoln, Nebraska).

758

759 **Graph Plots and Statistical Analysis.** Plots and diagrams were generated using GraphPad Prism  
760 v9 (GraphPad Software, San Diego, Ca) or custom-written MATLAB® scripts. Statistical significance  
761 was determined using a two-tailed un-paired Student's t-test. P<0.05 was considered statistically  
762 significant. \*\*\*\* indicates P < 0.0001.

763

764 Table S1. Annotation of ChIP-seq Data from ModEncode used in Fig. S3.

765 Table S2. Table depicting the distribution of ChIP-seq target genes for each TF parsed out into  
766 expression categories outlined in Fig. S3.

767 Table S3. *C. elegans* and yeast strains used this work.

768 Table S4. List of plasmids used in this work.

769

## 770 BIBLIOGRAPHY:

- 771 1. G.-J. Hendriks *et al.*, *Mol Cell* **53**, 380-392 (2014).
- 772 2. C. L. Araya *et al.*, *Nature* **512**, 400-405 (2014).
- 773 3. S. Brenner, *Genetics* **77**, 71-94 (1974).
- 774 4. A. G. Fraser *et al.*, *Nature* **408**, 325-330. (2000).
- 775 5. R. S. Kamath *et al.*, *Nature* **421**, 231-237 (2003).
- 776 6. D. J. Dickinson *et al.*, *Nature methods* **10**, 1028-1034 (2013).
- 777 7. J. E. Sulston, H. R. Horvitz, *Developmental biology* **56**, 110-156. (1977).
- 778 8. W. Keil *et al.*, *Developmental cell*, (2016).
- 779 9. D. Ershov *et al.*, *Nat Methods* **19**, 829-832 (2022).
- 780 10. P. James *et al.*, *Genetics* **144**, 1425-1436 (1996).
- 781 11. A. J. Walhout *et al.*, *Yeast* **17**, 88-94 (2000).
- 782 12. A. J. Walhout, M. Vidal, *Methods* **24**, 297-306 (2001).
- 783 13. J. S. Reece-Hoyes *et al.*, *Nat Methods* **8**, 1059-1064 (2011).
- 784 14. K. L. Borden, *Biochemistry and cell biology = Biochimie et biologie cellulaire* **76**, 351-358  
785 (1998).
- 786 15. Y. Zhang *et al.*, *Genome biology* **9**, R137-139 (2008).
- 787 16. N. Stec *et al.*, *Curr Biol* **31**, 809-826 e806 (2021).
- 788 17. C. Bieniossek *et al.*, *Current protocols in protein science* **Chapter 5**, Unit 5.20-25.20.26  
789 (2008).

790

791